Paper proposed for the 36th European Rotorcraft Forum,
7th to 9th September, 2010 - Paris, France

Performance Assessment of the Erica Tilt-Rotor in Cruise

Julien DECOURS [†], Stephane Burguburu [†], Fabrice Falissard [‡]
[†] ONERA Applied Aerodynamics Department
[‡] ONERA Computational Fluid dynamics and Aeroacoustics Department
BP 72, 92322 Châtillon Cedex, France
julien.decours@onera.fr, stephane.burguburu@onera.fr, fabrice.falissard@onera.fr

Key words: Tilt-rotor, Performance, Numerical simulation, Aerodynamics, Acoustics, Drag

Abstract: One of the numerous goals of the NICETRIP project (Novel Innovative Competitive Effective Tilt Rotor Integrated Project) is the assessment of the performance of the Erica tilt-rotor in aircraft configuration (Figure 1). After a description of the numerical methods, the blade root optimisation is described and the blade tip performance analysis is presented. Then, a drag analysis is done in cruise to identify the aircraft drag sources and to anticipate the Reynolds effects which will occur during the future tests in the LLF and S1MA wind tunnels. Finally, a full unsteady CFD calculation of the aircraft with propellers is presented. The unsteady blade pressures are then used as input data for the acoustic computations with the KIM code to assess the noise radiated on the cabin at M=0.50.

1 INTRODUCTION

A tilt-rotor is an aircraft which can combine both advantages of helicopter hovering capability and the high speed aibility of conventional airplanes thanks to the conversion of its nacelles, from the hover position (helicopter mode) to the cruise position (propeller mode). Thus, the development of the tilt-rotor technology is very attractive and it is important to estimate aerodynamic performance. Therefore, the European Union decided to launch several research programs funded within the framework of the 5th PCRD that aim at developing a new generation of tilt-rotors in Europe, based on the ERICA (Figure 1) half moveable wing concept proposed by AGUSTA [1].

ONERA research activity on tilt-rotor is continuing within the European funded NICETRIP program. An unsteady complete aircraft simulation has been performed in order to estimate the fuselage noise. A blade root optimization task in collaboration with Eurocopter Deutschland has also been done. Finally, a drag analysis has been done in cruise to identify the aircraft drag sources and to anticipate the Reynolds effects which will occur during the future tests in the LLF and S1MA wind tunnels.

The paper first presents the numerical methods used to perform the Navier-Stokes simulations. After that, we will focus on rotor blade performance simulations and optimization, drag analysis to finish with the complete aircraft simulation.

Figure 1: The ERICA tilt-rotor powered model

2 Numerical Methods

The ONERA object-oriented computational code *elsA* (Ensemble Logiciel de Simulation en Aérodynamique) solves the Reynolds averaged Navier-Stokes equations in a finite volume formulation on multiblock structured meshes. The solver is used for a large variety of configurations (aircraft, turbomachinery, helicopter, tiltrotor…). Concerning drag analysis, numerical simulations of the aircraft with actuator disk were performed at ONERA with this *elsA* software. Navier-Stokes computations were run with a quasi-steady approach to model the rotor, using an actuator-disk: the Chimera technique with overlapping grids was used to simplify the mesh generation. Concerning rotor blade optimization, numerical simulations of the scale 1 full span aircraft in cruise configuration were also performed at ONERA. Navier-Stokes computations were run with a steady approach to model the isolated rotor and the blade with spinner. Finally an unsteady approach was used to simulate the complete aircraft with his rotor. The Chimera technique was used to allow the rotation of the rotor.

2.1 Aircraft with actuator disk

The numerical parameters used to calculate the aircraft performance are based on a 2nd order Jameson scheme space discretisation with a scalar artificial viscosity including Martinelli's correction combined with a LU-SSOR scalar relaxation implicit phase with backward Euler time integration. Among the several turbulence models available in *elsA*, the Wilcox k-ω model with SST correction was chosen.

The simulation of a rotating machine (rotor, propeller…) can be simplified by modeling the rotor as a lifting surface, called "actuator disk". It represents the rotor loads which are averaged in time and applied on a surface grid in a steady flow computation. The actuator disk model is introduced into the code as a particular boundary condition where discontinuous aerodynamic quantities are prescribed. Due to the steady-state assumption, a large reduction of computational cost is achieved by comparison with an unsteady computation of the flow around rotating blades. The boundary condition formulation behaves like an usual interface and the actuator disk source terms are simply added to the residuals for the cells lying below the actuator disk surface. The source terms which model the discontinuities of the flow field are calculated by blade element theory with the HOST comprehensive analysis from Eurocopter allowing either a uniform global lift or evolutions in the radial and azimuthal directions on the disk (non-uniform actuator disk).

The construction of a multi-block mesh around complex geometries is difficult and needs a good know-how. The Chimera technique allows simplifying the process of mesh generation by using a background grid, on which can overlap additional body parts. The technique consists in introducing classical overlapping boundary conditions and also masks conditions around solid areas which will influence the overlapped grids.

2.2 Isolated rotor simulation

The isolated rotor has been simulated with a quarter cylinder mesh around a single blade (Figure 2). The spinner has been modeled by the inner cylinder with a 'wallslip' Euler boundary condition. Periodic boundary conditions are set on the two periodic faces and a 'farfield' boundary condition has been set on all over external surfaces. A Navier-Stokes adiabatic wall condition has been set on the blade surface. The whole mesh rotates into an upstream uniform wind. An 'O' grid meshing topology has been used in order to limit the global grid size and to ensure a very good nodes distribution and orthogonality in the vicinity of the blade. The blade has been fairly well discretized in terms of chord and normal distribution, but also in the spanwise distribution, especially in the blade root and tip area. The single blade grid contains a total of about 1.8 million nodes distributed in 8 blocks. The full scale blade radius is 3.7m, rotational speed is 426RPM in cruise, and cruise speed is 300kts corresponding to a Mach number equal to 0.5. One computation (fixed pitch) requires about 3h CPU time on a NEC SX8 computer.

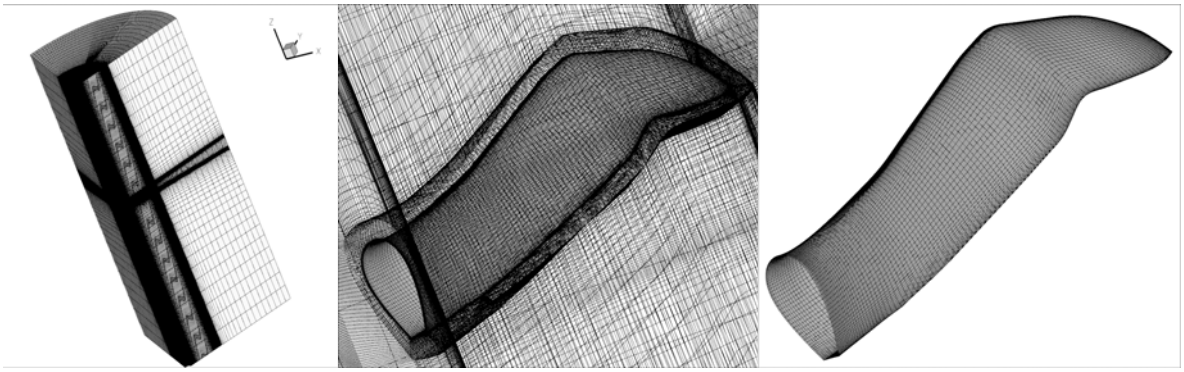

Figure 2: Single blade ‘O’ topology and skin mesh

2.3 Blade with spinner

Following Eurocopter Deutschland investigations, it has been decided to compute the blade root performance with the complete spinner geometry in order to evaluate the spinner effect on the blade performance. Therefore, Eurocopter Deutschland has provided his spinner grid to ONERA and ONERA has adapted his blade grid to the Chimera technique. The spinner grid, including the hole in the spinner and the yoke is presented in Figure 3 with the Chimera blade grid including the root and the cylinder part. The complete mesh system is also presented in Figure 3 with a colour for each part of the system.

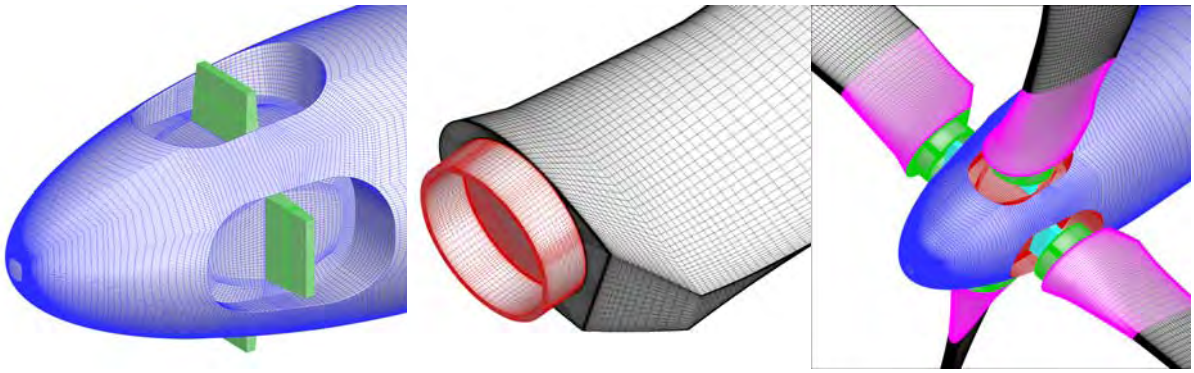

Figure 3: Spinner mesh from Eurocopter Deutschland and blade root with cylindrical part and cut at the trailing-edge

2.4 Complete aircraft simulation

In order to ease the construction of a mesh around a complete aircraft, the Chimera technique has been used, with the fuselage as a background grid, on which the rotor is overlapped. The grid has been realized by ONERA (based on a topology proposed by POLIMI) with the ICEM-CFD software. The ‘long tail’ half fuselage background grid contains a total of about 9 Million points distributed in 21 blocks with a first cell size of 2 microns (Figure 4). Each blade has been meshed with an ‘O’ topology (coming from the single blade mesh) and contains a total of about 1 Million points distributed in 8 blocks. The blade mesh has been adapted in order to avoid the necessity of masking the wing, the air intake and the nacelle in the blade grid. Therefore a gap has been modeled between the blades and the spinner, in addition to a split of the rotor mesh just before the air intake. The computations require about 36h CPU time per revolution on a NEC SX-8 computer with a time step of 2°. Three revolutions were required to reach the convergence.

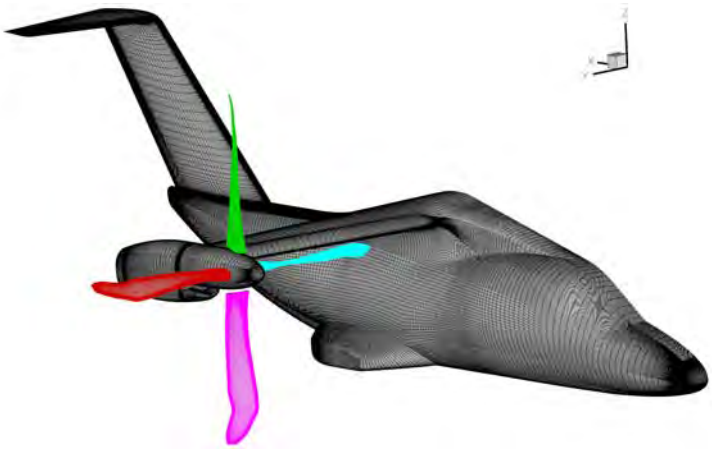

Figure 4: Half aircraft and rotor skin meshes

3 Flow Solutions and discussion

3.1 Blade root optimization

The blade root optimization study has been done on in collaboration with Eurocopter Deutschland. A first blade root has been proposed by ONERA in mid 2008 and chosen as the new starting point of the optimization, depending on structural constraint evolution. Compared to the original ADYN blade root the first shape allows avoiding any flow separation (Figure 5). This blade root lead to 8% efficiency increase in high speed flight configuration, in addition to the suppression of any loads fluctuation responsible for blade vibrations.

The rotor is assumed to develop a thrust of about 7700N in cruise flight with a high efficiency and a pitch of 53°. It appears that both the blade root and the blade tip have an important effect on the thrust and its efficiency in high speed flight. The blade tip is highly loaded because of the important rotational speed and so is the blade root because of its important relative thickness compared to the cruise flight advancing speed.

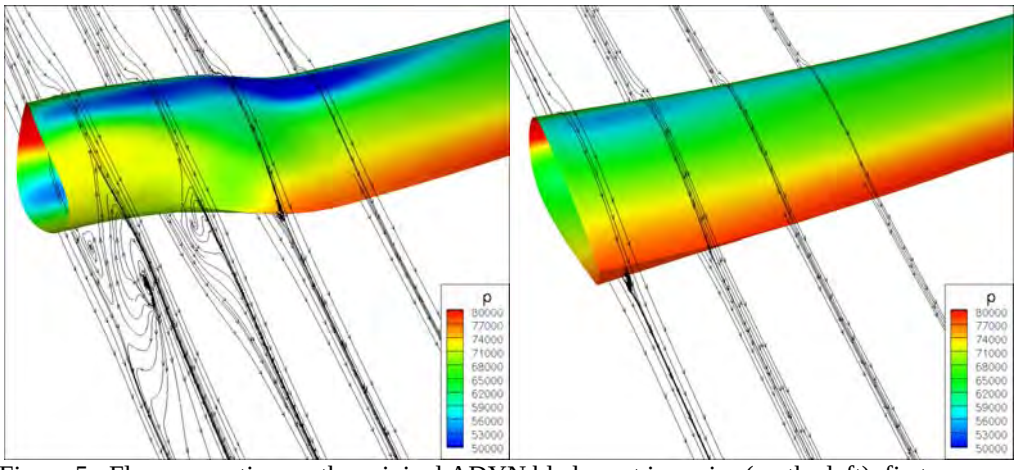

Figure 5 : Flow separation on the original ADYN blade root in cruise (on the left), first proposed blade root (on the right).

After that, new constraints have been proposed by the NICETRIP partners corresponding to a larger blade root associated to a cylinder making the junction between the spinner and the blade root (Figure 6). This new shape leads to important flow separation and loads fluctuations behind the cylindrical part and the blade root in addition to a loss of efficiency of about 8 counts.

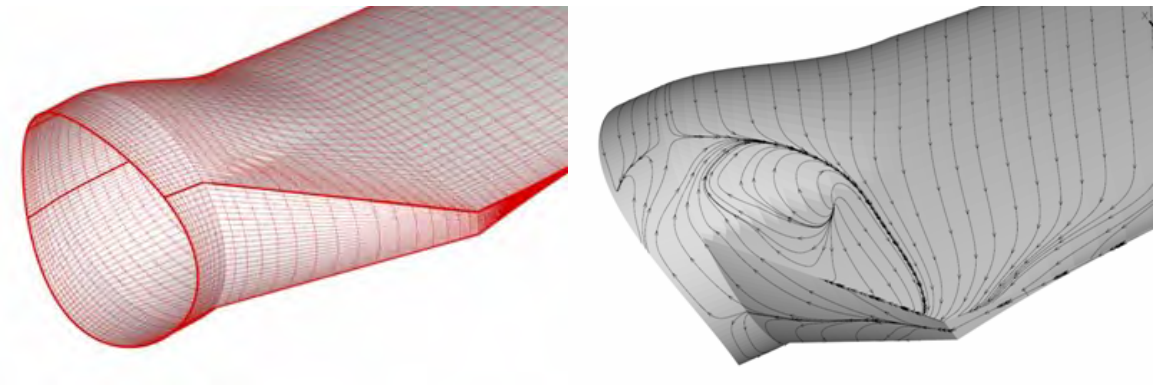

Figure 6: Blade root mesh (on the left) and skin friction lines on the right

Therefore, ONERA has proposed a new shape responding to those constraints and avoiding unsteady flow separation and loads fluctuation generating blade vibration (Figure 7). Those simulations have been done on the realistic spinner proposed by Eurocopter Deutschland in order to take into account the spinner effect on blade performance. The aerodynamic part of the blade (in black Figure 7) present a high efficiency for 7700N thrust, but when the blade root (in pink Figure 7) is added, the blade efficiency decreases by about 8 counts. The cylindrical part also generates a drag of about 650N corresponding to 8.4% of the rotor thrust. Finally, the junction between the blade and the spinner should also be optimized because it could generate a dramatic loss of efficiency of the complete propulsion system when flying at Mach 0.5.

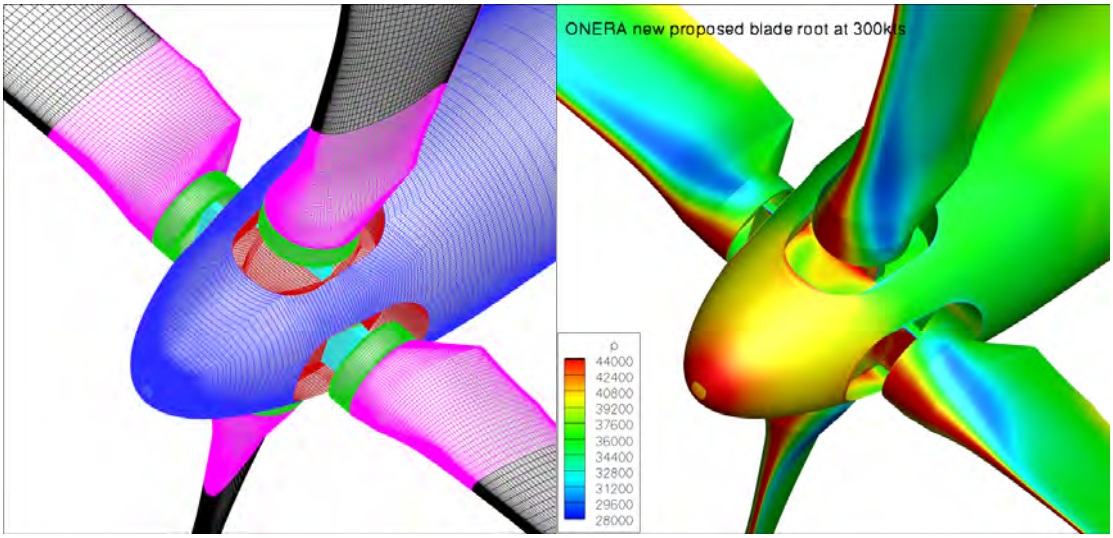

Figure 7: Complete mesh system and pressure distribution in cruise for the final ONERA blade root

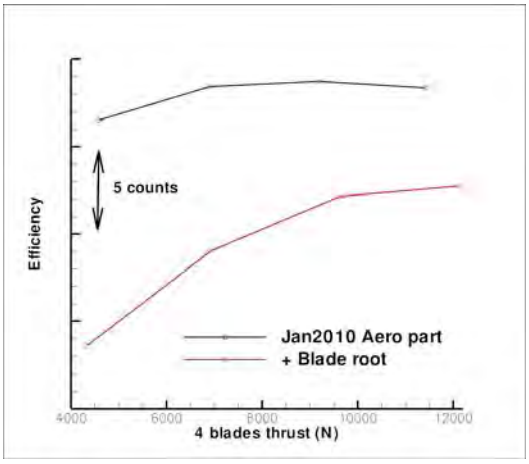

Figure 8: Performance breakdown in cruise

3.2 Blade tip cruise efficiency

After the blade root, the blade tip efficiency has also been analysed by ONERA. Therefore, thrust and drag distributions along the span on the geometry proposed by ONERA for different pitch angles (nominal pitch in black) are presented in Figure 9. The local efficiency is plotted on the aerodynamic part of the blade in addition to skin pressure and airfoil distributions in Figure 10. This curve shows that a non negligible loss of efficiency occurs between r/R=0.7 and r/R=0.85. The plotted airfoil distribution suggests that the interpolation effect between OA312 and OA309 airfoils should not be the main reason for this loss of efficiency, since the transition zone is located beyond the section of the minimum local efficiency. On the other hand, the sweep distribution which has its maximum located at r/R=0.788 can be suspected to be responsible for this loss of efficiency. At r/R=0.788 there is a sweep law inversion with a chord decrease in addition to a relative thickness sudden decrease from 12% at r/R=0.788 to 9% at r/R=0.862. This generates a kind of 3D surface bump on the leading edge located at r/R=0.788, exactly where the normal Mach number is maximum because of the sweep law inversion.

To sum up, we suspect a combination of sweep law inversion in addition to chord and relative thickness decrease to generate this important loss of efficiency. Modified sweep and chord laws could be investigated in order to estimate the potential in limiting this local loss of efficiency.

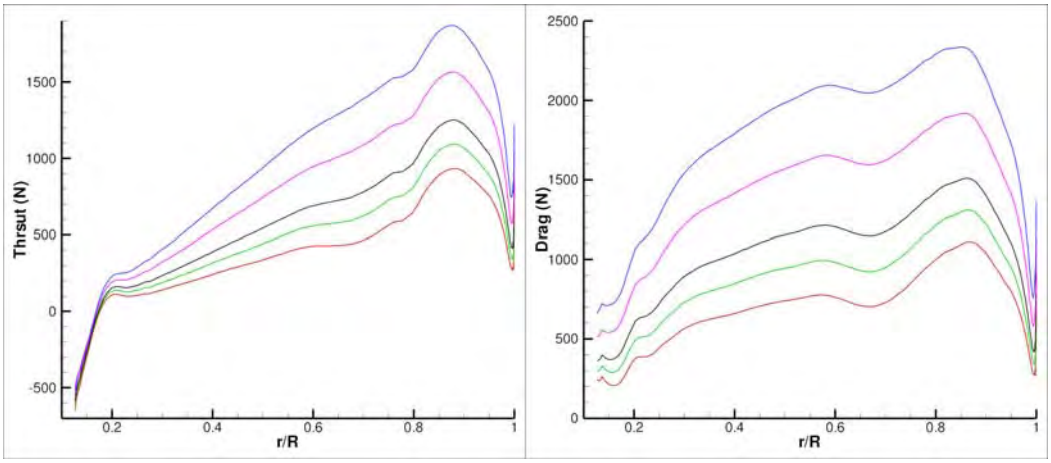

Figure 9: Thrust and drag distribution on the geometry proposed by ONERA for different pitch angles (nominal pitch in black)

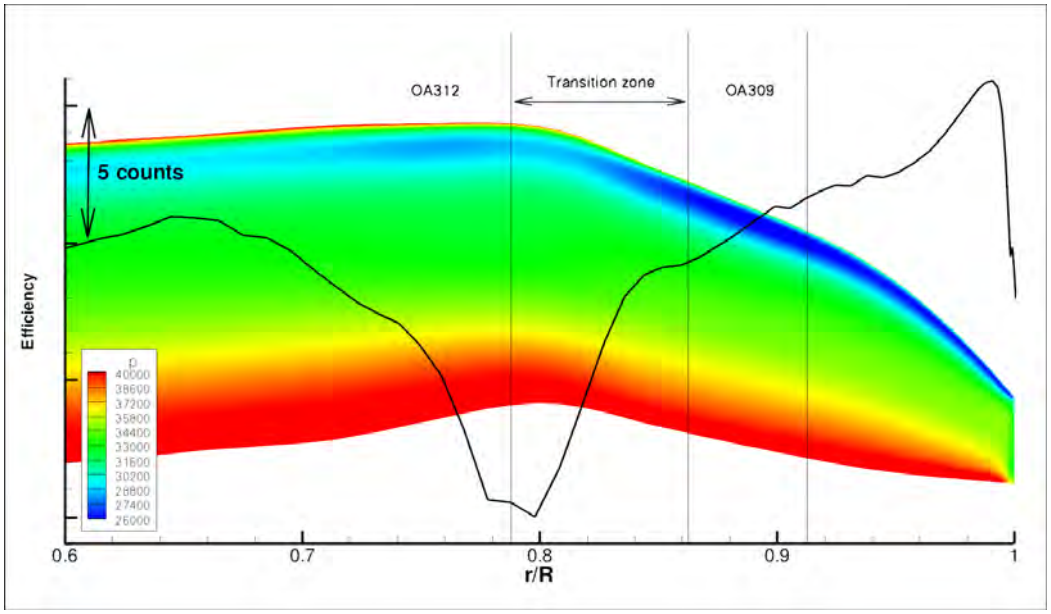

Figure 10: Efficiency distribution on aerodynamic part of the blade for the geometry proposed by ONERA at nominal pitch, skin pressure and airfoil distribution

3.3 Drag analysis

During steady level flight, the propeller thrust must balance the aircraft drag. As the studied configuration is unusual compared to classical aircraft, the number of reference data to compare with are low. For that reason, a special attention is paid to the drag which can be assessed by to ways:

- The near field approach, which consist in integrating pressure and friction around all solid parts of the aircraft
- The far-field approach which is based on the momentum analysis downstream of the aircraft assuming a uniform upstream flow field.

The near-field technique is known to be reliable for lift but not always for drag. Indeed, the drag is 10th to 30th lower than lift and a lack of accuracy on it has a direct impact on the aircraft performance. Moreover, the drag is very sensitive to numerical errors, and thus sensitive to the mesh density. As no mesh convergence is done in the present case, a far-field technique (called FFD, [8]) is used here to asses the accuracy of the drag provided by the near-field approach. In addition, the far-field analysis gives the drag breakdown (viscous, wave and lift-induced drag) which are important information for designers.

The far-field technique relies on the momentum theorem and mass conservation [8], [9] which defines the vector $\vec{f}$:

$$\vec{f} = -\rho(u-u_\infty)\vec{q} - (p-p_\infty)\vec{i} + \vec{\tau}_x$$

All the field quantities involved in the far-field technique are based on the velocity defect $\Delta\overline{u}$ which can be expressed as:

$$\Delta\overline{u} = u_\infty \sqrt{1 + \frac{2\Delta H_i}{q_\infty^2} - \frac{2[\left(e^{\frac{\Delta s}{r}}\right)^{\frac{\gamma-1}{\gamma}} - 1]}{(\gamma-1)M_\infty^2}} - u_\infty$$

This equation gives the velocity defect in a flow which recovers the freestream pressure downstream of the body. The irreversible phenomena issued from the shear layers and the shocks are represented by the two thermodynamics terms Δs (entropy variation) and ΔH_i (enthalpy variation). Only for illustration, the velocity defects is represented downstream of the aircraft in Figure 11.

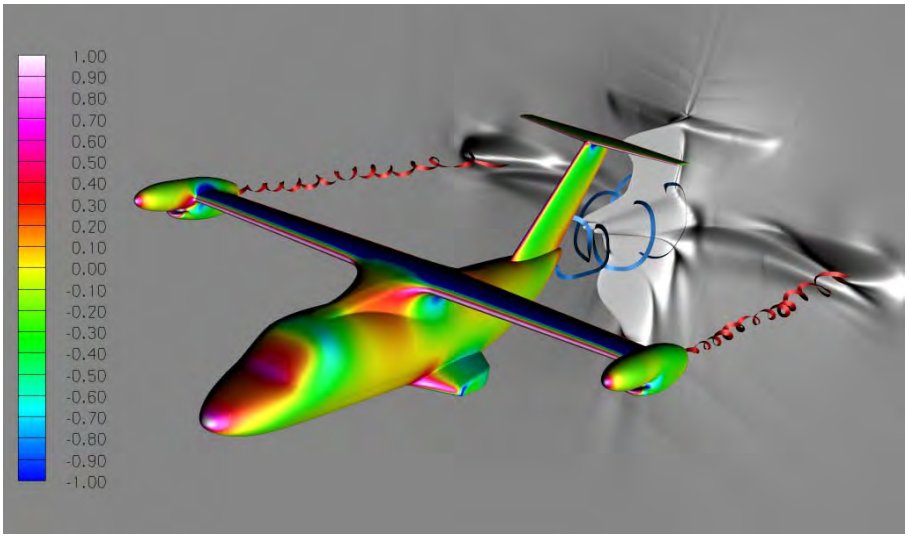

Figure 11 – Velocity defect downstream of the aircraft (field=Kp)

The viscous drag D_v and wave drag D_w are related to irreversible phenomena and can be expressed by the following expressions:

$$\begin{cases} D_v = \int_{Vv} div\vec{f}_{vw} dV \\ D_w = \int_{Vw} div\vec{f}_{vw} dV \end{cases} \quad \text{with} \quad \vec{f}_{vw} = -\rho\Delta\overline{u}\vec{q}$$

These two relations only differ by their integration volumes which are defined in Figure 12 .

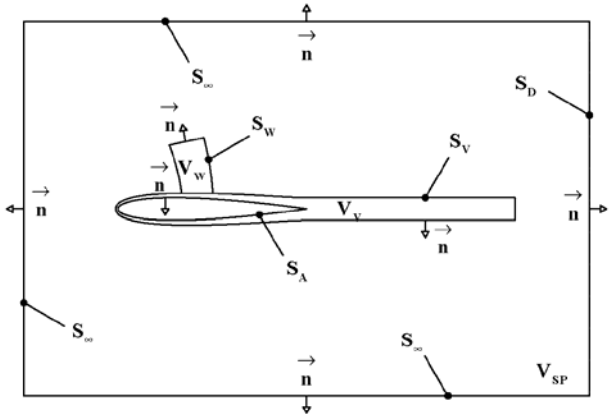

Figure 12 – Boundaries and control volumes for far-field drag breakdown

Outside of these volumes V_v and V_w, the flow is assumed to be inviscid: this is checked a-posteriori as shown in Figure 13 (only viscous volume: as no shock occurs within the flow, the wave drag is equal to zero).

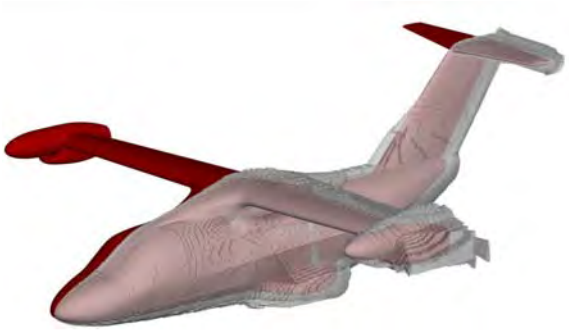

Figure 13 – Control volume for viscous drag

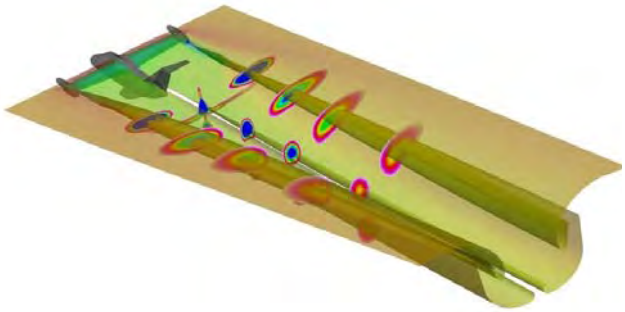

Figure 14 – Illustration of the apparent lift-induced drag
(Scale 1:1, low speed AC1, α=10°)

The lift-induced drag is related to reversible phenomena which occur when a lift is created such as trailing vortices. Figure 14 represents the freestream surface downstream of the aircraft at high incidence (AC1, M=0.1763, α=+10°, C_l=1.41). This figure clearly highlights the huge vorticity generated by the high lift, and thus 100 m downstream of the aircraft.

The definition of the induced drag slightly differs from the previous definition of the viscous and wave drag. One defines $\vec{f}_i$ such that $\vec{f} = \vec{f}_{vw} + \vec{f}_i$ and the momentum equation is written:

$$\vec{f}_i = -\rho(u - u_\infty - \Delta\overline{u})\vec{q} - (p - p_\infty)\vec{i} + \vec{\tau}_x$$

In the case of a non-propelled aircraft, the lift-induced drag is given by:

$$D_i = \int_{Vi} div\vec{f}_i dV - \int_{S_A} (\vec{f}_i \cdot \vec{n}) dS$$

The far-field approach is applied to calculate the drag on the two configurations calculated at M=0.50. The summary of the results are given in Table 1 hereafter.

			Near-field (Cd 10^{-4})				Far-field (Cd 10-4)					
Scale	Mach Number	Re 10^6	Cd pressure	Cd friction	**Total Cd**	**Drag (N, 1/2 aircraft)**	Cd Viscous pressure	Cd Wave	Cd Lift-induced	Cd Spurious	**Total Cd**	**Drag (N, 1/2 aircraft)**
1:1	0,5	12,4	359	172	**532**	**6235**	133	0	210	17	**516**	**6046**
1:5	0,5	4,9	382	223	**606**	**555**	168	0	198	16	**589**	**540**

Table 1 – Drag breakdown (near filed and far-field approach)

When passing from scale 1:1 to scale 1:5, the near-field lift is decreased by 4% and the near-field drag increases by 14% as expected. One notices that the drag generated by the friction is about 35% of the total drag, which is quite low compared to more "classical" aircraft where the pressure drag is usually less than the friction drag. The presence of closed nacelles may explain the high value of the pressure drag.

The drag breakdown given by FFD also indicates a 14% increase of the drag when comparing the scale 1:1 to the scale 1:5. It is also noticed that a lift-induced drag comprises between 33% and 40% of the total drag, to be compared to the theoretical value $\frac{C_l^2}{\pi\lambda}$. In this formula, λ is the wing aspect ratio and is defined by $\lambda = \frac{b^2}{S}$ with *b* wing span and *S* wing surface. With the Erica scale 1:1 datum, the theoretical drag is $\frac{0.4919^2}{\pi \frac{14^2}{35}} = 0.0137$, which is far below the actual value given by FFD (~0.0200). The most probable explanation is the presence of the fuselage, of the nacelle and the elevator which all participate to the lift and thus amplify the lift-induced drag.

The difference between the near-field and the far-field drag is the so-called spurious drag and is equal to 16.10^{-4} for both scales. As the Mach number, the numerical scheme, the mesh and all numerical parameters are unchanged, this spurious drag remains remarkably constant and represents about 3% of the total drag. This gives the accuracy of the near-field approach and thus increases the confidence of all the presented results.

Finally, it can be claimed that the thrust to be delivered by the propeller must be –at least- equal to 6040N. The next paragraph will discuss on the installed performance which differs from this presented isolated aircraft configuration.

3.4 Complete aircraft unsteady simulation

The blade pitch of 53° has been chosen to simulate the complete aircraft in cruise in order to address the cabin noise problem. In this time accurate simulation, particular attention has been paid to the unsteady load fluctuations on the fuselage and on the blades.

Concerning the half aircraft drag, Figure 15 presents about 6% fluctuation with a mean value of 5800N. The maximum drag corresponds to the passage of a blade in front of the wing. The drag value could be compared to isolated aircraft results, without actuator disk in the same cruise condition. This simulation presents a near field drag of 6290N and a far field post treatment drag of 6040N. Therefore, the rotor is responsible for a drag decrease of about 8% compared to the isolated half aircraft. Concerning the half aircraft lift, Figure 15 presents about 2% lift fluctuation with a mean value of 62500N. The maximum lift also corresponds to the passage of a blade in front of the wing. Isolated half aircraft simulation presents a near field lift of 57640N and the weight of the aircraft is 10870kg corresponding to 53260N for the half aircraft. The rotor swirl is responsible for a lift increase of about 8% compared to the isolated half aircraft.

Concerning the rotor, the four blades thrust and efficiency are plotted in Figure 16. The total thrust is about 7300N with 19% 4/rev oscillations and the total efficiency presents 3.6% 4/rev

oscillations around the mean efficiency value. The 2.9% loss of efficiency compared to previous isolated rotor simulations are due to installation effects, especially because of the rotating flow generated around the wing and the nacelle (finite span effect).

Each blade thrust during the third rotor revolution is presented in Figure 17. The black curve (blade n°1) goes from a maximum thrust of about 3150N between Ψ=45° and Ψ=65° to a minimum negative thrust of about -100N at Ψ=128°. This very large thrust variation can not be caused by the axial velocity perturbation generated by the wing (Figure 18) because this perturbation is weak in the rotor disk region (about 3% of the aircraft speed). On the contrary, the azimuthal velocity perturbation has an important effect on each blade thrust. In the yellow circle in Figure 19 the azimuthal velocity relative to the aircraft speed is about 3% but the direction is opposite of the blade rotational speed. Therefore the blade angle of attack is increased and the thrust consequently (about 3150N between Ψ=45° and Ψ=65°). In the red circle in Figure 19 the azimuthal velocity relative to the aircraft speed is about 6% and the direction is the same as the blade rotational speed. Therefore the blade angle of attack is dramatically decreased and the thrust consequently (about -100N at Ψ=128°). Figure 20 presents the iso-contours of the Q criteria, for a rotor position corresponding to minimum thrust for one blade (Ψ=128°). Many vertical structures including each blade tip vortex are visible, even if it is clear that the grid resolution is not fine enough to capture very accurately the structures in the entire computational domain.

Finally, the unsteady pressure distribution on blade skins, calculated each 2° of azimuth, are used as input data for the acoustic computations with the KIM code based on the solid surface formulation of the Ffowcs Williams and Hawking equation [10]. The Over All Sound Pressure (OASPL) levels computed on the fuselage are presented in Figure 21. In this figure, the OASPL obtained from the full aircraft computation are compared with OASPL obtained from the computation of the isolated propeller in the same flight conditions. Depending on the microphone position, an increase of the noise level by 8 to 20 dbA is observed when the full aircraft is modelled. The higher acoustic levels observed in the case of the full aircraft computation are due to the impulsive loading fluctuation, observed on the propeller blade, resulting from the flow distorsion induced by the aircraft wing and fuselage. Indeed, this induced velocity slightly modifies the blade incidence as a function of the blade position and creates a load oscillation of ±100% of the mean load. A cyclic pitch control command might be useful to compensate this important loss of angle of attack and associated thrust.

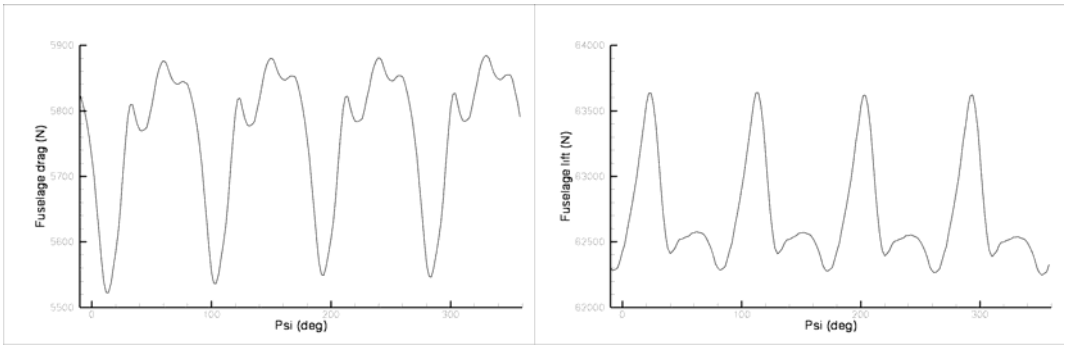

Figure 15: Aircraft drag and lift during the third rotor revolution

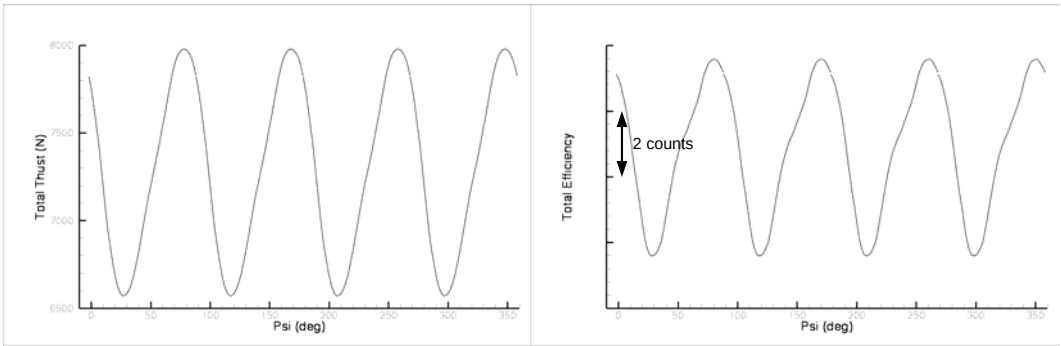

Figure 16: Rotor thrust and efficiency during the third rotor revolution

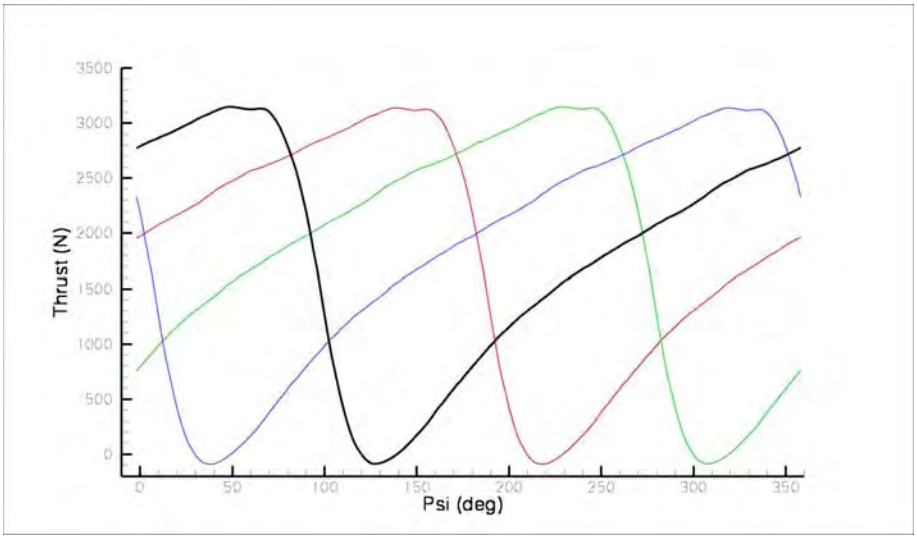

Figure 17: Each blade thrust during the third rotor revolution

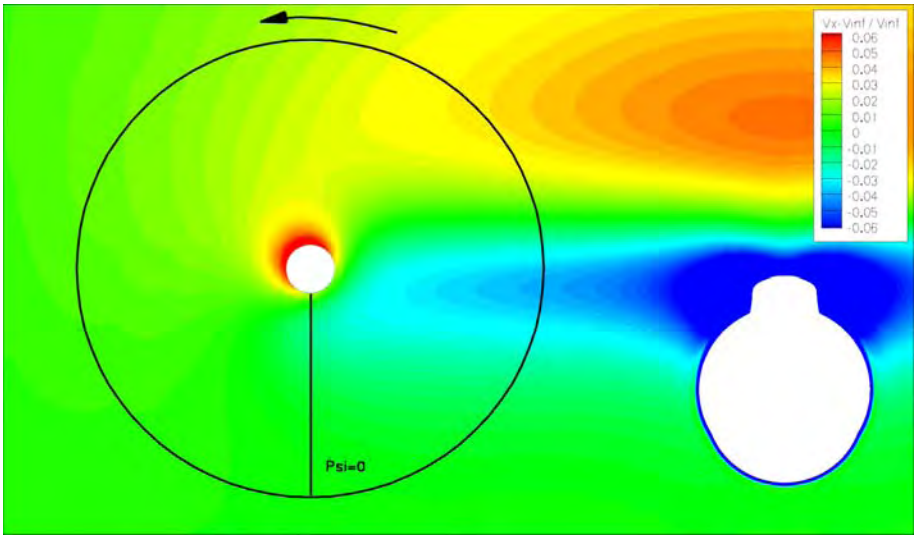

Figure 18: Axial velocity perturbation relative to the aircraft speed in the rotor plane

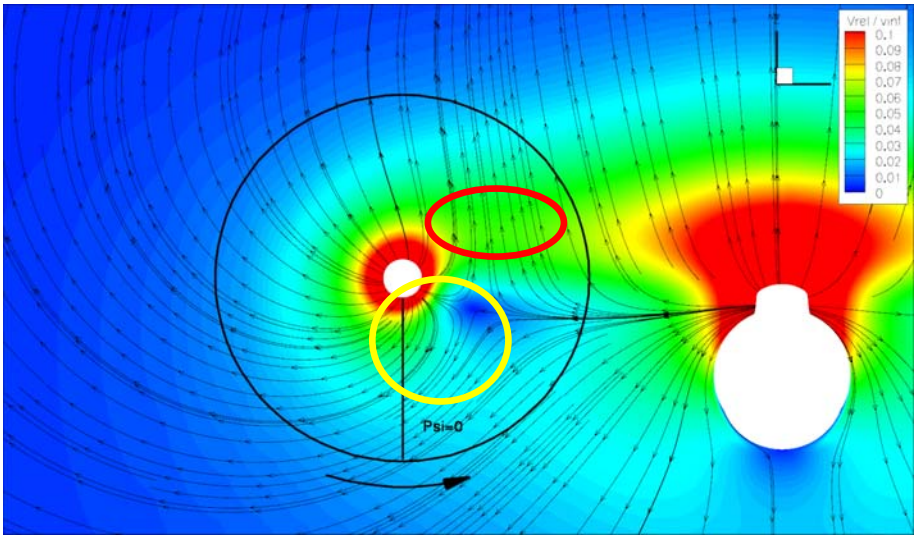

Figure 19: Azimuthal velocity perturbation relative to the aircraft speed in the rotor plane and streamtraces. Benefit in the yellow zone, important loss of AoA and thrust in the red zone.

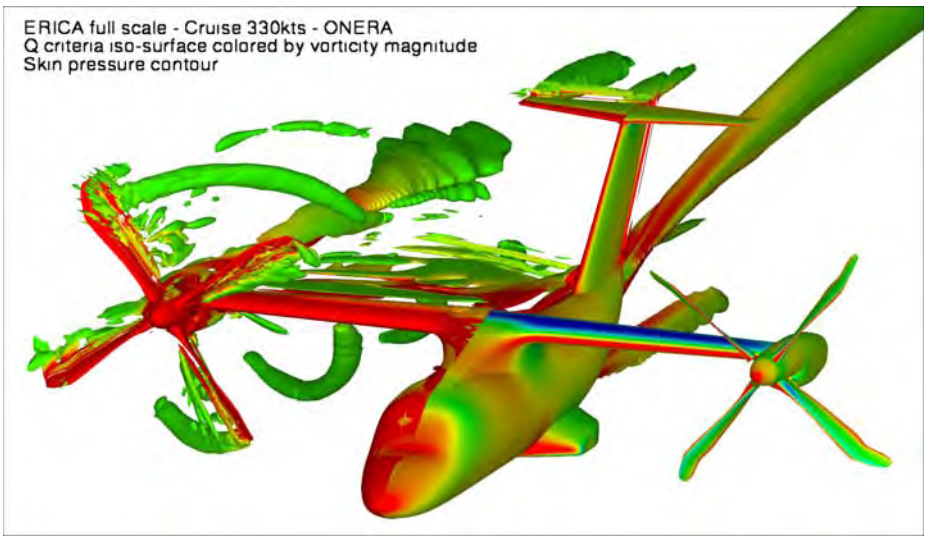

Figure 20: Q criteria iso-contours at the minimum single blade thrust rotor position

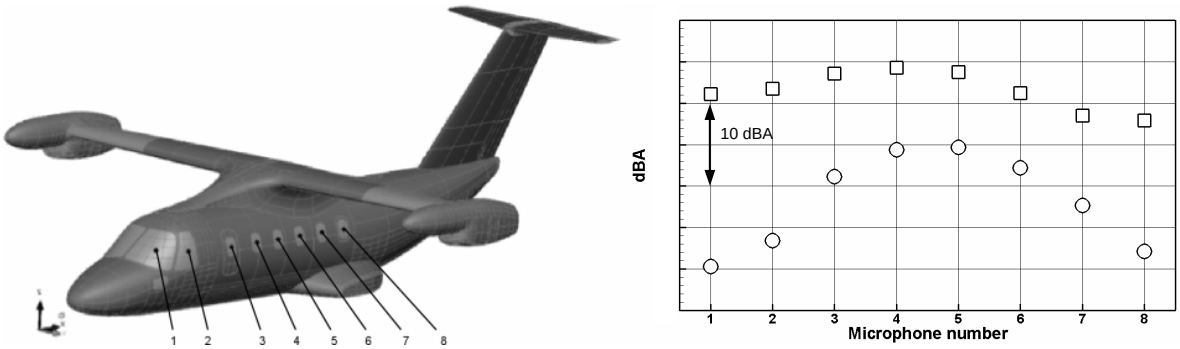

Figure 21: Microphone locations on the fuselage (on the left) and noise levels at microphone locations for full aircraft (□) and isolated propeller (○) computations (on the right).

4 Conclusion

ONERA has performed complex simulations of various configurations based on the ERICA concept, from steady isolated blade performance estimation to complete aircraft unsteady simulation. These simulations allow good performance estimation. The blade root optimization has already shown that 8% efficiency increase, compared to the ADYN tested geometry, is reachable with loads fluctuations and associated vibration suppression. It has been shown that the blade tip could also be further optimized. The drag analysis based on the far-field approach shows an important lift-induced drag compared to classical aircraft. Nevertheless, the computed drag is close to the previous estimations based on a near-field approach and thus the targeted propeller thrust does not much differ from first estimations. Finally, the simulation performed within the NICETRIP noise task T1.2.5 was the first unsteady Navier-Stokes simulation done at ONERA taking into account the complete aircraft. Important installation effects have been shown, mainly due to the lift and associated swirl generated by the wing. Along one rotor revolution the blade thrust oscillates from a negative value (about -100N) to a highly loaded value (about 3150N) compared to isolated blade steady thrust (about 1925N). This loss of thrust is associated with a 3% loss of efficiency for the isolated blade. It as also been shown that this load fluctuation generates an increase of the noise level by 8 to 20 dbA, depending on the microphone position. As a continuation, it can be recommended to adapt the blade sweep law to high speed flight and to elaborate a cyclic (or multi-cyclic) pitch control law which would reduce the unsteady loads. This technique should be able to increase the propeller efficiency and reduce the cabin noise in cruise flight.

References

[1] F. Nannoni, G. Giancamilli, M. Cicalè, *"ERICA: The European Advanced Tiltrotor"*, 27th European Rotorcraft Forum, Moscow (Russia), September 11-14, 2001

[2] Visingardi, A., Khier, W., Decours J., *"The Blind-test activity of TILTAERO project for the numerical aerodynamic investigation of a tilt rotor"*, IV Eccomas Congress, Jyväskylä, SU, July 2004.

[3] Visingardi, A., Khier, W., Decours J., Voutsinas S.*"Code to code comparisons for blind test activity of the TILTAERO project"*, 31st European Rotorcraft Forum, Firenze, Italy, September 2005

[4] Lefebvre T., Beaumier P., Canard S., Pisoni A., Pagano A., van der Wall B. , D'Alascio A., Arzoumanian C., Riziotis V and Hermans C,. *"Aerodynamic and aero acoustic optimization of modern tilt rotor blades within the ADYN project"*, IV Eccomas Congress, Jyväskylä, SU, July 2004

[5] P. Beaumier, Y. Delrieux, *"Description and validation of the ONERA computational method for the prediction of blade-vortex interaction noise"*, 29th European Rotorcraft Forum, Friedrichshafen (Allemagne), September 16-18, 2003

[6] J. Decours, T. Lefebvre, *"Navier-Stokes computations applied to tiltrotors"*, 33rd European Rotorcraft Forum, Kazan, September 11-13, 2007

[7] P. Beaumier, J. Decours, T. Lefebvre, *"Aerodynamic and aero-acoustic design of a modern tiltrotor: the ONERA experience"*, 26th ICAS Congress, Anchorage, Alaska, USA, 14-19 September 2008

[8] D. Destarac, *"Drag Extraction from Numerical Solutions to the Equations of Fluid Dynamics : the Far-field 'Philisophy' "*, Conference AAAF No43.

[9] S. Esquieu, *"Reliable Drag Extraction From Numerical Solutions: Elimination of Spurious Drag"*, NATO Symposium AVT 147, Dec. 3rd – 6th, 2007, Athens, Greece.

[10] J. Prieur and G. Rahier, *"Comparison of Ffowcs Williams-Hawkings and Kirchhoff rotor noise calculations"*, AIAA Paper 98-2376, 1998.